Environmental Challenges 5 (2021) 100240

Contents lists available at ScienceDirect

Environmental Challenges

journal homepage: www.elsevier.com/locate/envc

Adsorptive and photocatalytic performance of perovskite material for the removal of food dye in an aqueous solution

Sushmita Banerjee [a,*], Abhijit Debnath [b], Bharat Kumar Allam [c], Neksumi Musa [a]

[a] Department of Environmental Science, School of Basic Sciences and Research, Sharda University, Greater Noida, India
[b] Department of Civil Engineering, Indian Institute of Technology (BHU), Varanasi, India
[c] Department of Chemistry, Faculty of Basic Sciences, Rajiv Gandhi University (A Central University), Rono Hills, Arunachal Pradesh, India

ARTICLE INFO

Keywords:
Perovskite
Food dye
Adsorption
Mass transfer
Photocatalytic degradation

ABSTRACT

Lanthanum cerate ($La_2Ce_2O_7$), a perovskite nanomaterial, has been synthesized by using the gel combustion method to remove carcinogenic and neurotoxic dye FD&C Yellow 5 from its aqueous solution and the same has been also explored to investigate the photocatalytic behavior towards the degradation of food dye. The synthesized material has been extensively characterized using various techniques such as XRD, FT-IR, SEM, BET surface area and through pH_{ZPC}. The effect of various operational parameters like solution pH, temperature, and initial dye concentration were investigated to explore the optimum dye removal percentage. To gain the mechanistic perceptive of the dye removal process, various kinetic models were used. Pseudo-second order kinetic model was found to be well suited in describing the sorption system. The intra-particle diffusion model suggested that the film diffusion process controls the overall rate of the dye and perovskite interaction process.

Further, equilibrium data interpretation was appraised through various isotherm models and adsorption data found to be consistent with the Freundlich model suggesting multilayer coverage of dye species over the surface of perovskite particles and maximum adsorption capacity was evaluated as 133.3 mg/g at 323 K. Thermodynamic parametric investigation indicated that the dye adsorption process was feasible, spontaneous and endothermic. The activation energy of the adsorbate-adsorbent interaction process was found to be 5.26 kJ/mol, suggesting a physisorption mechanism governs the adsorption process. Photocatalytic efficiency of the perovskite was also scrutinized for dye concentrations 10, 25 and 50 mg/L and dye degradation of 89%, 75% and 69% was observed for each tested concentrations, respectively.

1. Introduction

Every day, a million liters of wastewater are generated globally result of various industrial and agriculturally based activities. However, the stringent regulation imposes by the government of multiple countries prohibited the regular practice of direct discharge of contaminated water into the natural water bodies. Therefore, it becomes mandatory to treat the wastewater before its release into nearby hydric resources. Dyes are among the most common organic water pollutants that can be easily perceived even when they present in minute amounts (Preeti et al., 2021). Several treatment methods are available for dye removal from aqueous solutions. Still, adsorption is considered a promising treatment technique among researchers for many decades because of its simplicity with excellent removal efficiency and low energy requirements. Ranges of adsorbent include agricultural wastes, activated carbon derived from agricultural wastes, clay, alumina, layered double oxides, iron nanoparticles, iron graphene composite etc. have been reported with outstanding discoloration efficiency.

Undoubtedly, physical and chemical properties of the adsorbent material such as surface area, pore-volume, porosity, density, particle size, pH_{ZPC}, presence of functional groups, charge, etc., controlled the adsorption process significantly. This motivated many researchers to design and fabricate new materials by controlling the physical and chemical characteristics of the adsorbent in such a manner that enhanced the pollutant scavenging efficiency to several folds. In the series of novel materials, perovskite oxide emerges as a new class of adsorbent material that attracted the scientific community's attention for its use in water and wastewater treatment. Perovskite materials are typically mixed metal oxides with the stoichiometry of ABX_3, where 'A' and 'B' are two cations of very different ionic radii and 'X' is the anion (oxide ion) that surrounds B (Mehdizadeh et al., 2020). This kind of stoichiometric arrangement results in a typical cubic structure (Jiang et al., 2003). These com-

* Corresponding author.
E-mail address: sushmita.banerjee@sharda.ac.in (S. Banerjee).

https://doi.org/10.1016/j.envc.2021.100240
Received 1 July 2021; Received in revised form 2 August 2021; Accepted 11 August 2021

pounds are receiving considerable attention due to their unique physical and chemical properties. Therefore, these mixed metal oxides are used as catalysts for several chemical reactions such as oxidation of hydrocarbons, exhaust gas depollution, hydrogenation, hydrogenolysis, photodecomposition, electrochemical decomposition, etc. (Védrine, 2019; Saeed et al., 2021). In the present study performance of lanthanum cerate ($La_2Ce_2O_7$) has been explored for the removal of carcinogenic and neurotoxic dye FD&C Yellow 5 from its aqueous solution.

The dye is known to be used extensively by food, cosmetics and pharmaceutical industries (Deepika et al., 2017; Sellaoui et al., 2021). However, during the production process and operation, a significant amount of dye escaped and flushed out along with industrial effluents and imparted objectionable color to the effluents. These untreated colored effluents are further responsible for the critically fouling of the aquatic ecosystem. Hence, removal of these undesirable colored nuisances from the waste streams is highly warranted. The adsorption potential of ceria is well recognized and documented by several researchers (Wei et al., 2019). Because of continuous flipping between Ce^{3+} and Ce^{4+} oxidation states, the ceria based system exhibit superior surface properties (Eriksson et al., 2018). In this study, mixed oxides of lanthanum and cerium have been used to anticipate that ceria doped lanthanum is endowed with enhanced surface chemistry and improved physical properties, which facilitates rapid uptake of the contaminants from the aqueous media. Further, the synthesized perovskite material has been also explored to investigate the photocatalytic behavior towards degradation of food dye.

2. Experimental

2.1. Adsorbate

Food dye, F&C Yellow 5 (analytical grade, purity content greater than 85%), having a chemical formula of $C_{16}H_9N_4Na_3O_9S_2$ and molecular weight of 534.37 g/mol, was obtained from Alfa Aesar (Thermo Fisher Scientific) India with CI no. 19,140 (mono-azo class), λ_{max} 425 nm and pKa value of 9.4. Stock solution of the model dyeing pollutant was prepared by dissolving 1.0 g of dye in 1 L of double-distilled water, and it was appropriately diluted to obtain the standard solutions of various concentrations (10–200 mg/L). The molecular structure of the dye is depicted in Fig. 1.

2.2. Chemicals

Analytical grade chemical reagents were used in the study and were employed in the reactions without further purification. Metal nitrate salts including lanthanum nitrate hexahydrate, cerium nitrate hexahydrate purchased from Alfa Aesar (Thermo Fisher Scientific) India, citric acid monohydrate (Loba Chemie Pvt. Ltd, India), ethylene glycol (Merck, Emplura grade, India), HCl (Merck, India), NaOH (SD Fine Chem Ltd., India).

2.3. Adsorbent synthesis

The synthesis of La-Ce mixed metal oxide was carried out using gel combustion-based modified Pechini method with minor modifications (Stoyanovskii et al., 2020; Dimesso, 2018). For synthesis, the metal precursors $La(NO_3)_3{\cdot}6H_2O$, $Ce(NO_3)_3{\cdot}6H_2O$ in a 1:1 stoichiometric ratio were dissolved in distilled water and stirred for 45 min at 70 °C to produce a homogenous transparent mixed metal nitrate solution. Later on, this mixed metal solution was added with citric acid by maintaining the metal to citrate ratio as 1:3, and the solution was kept for stirring for another 40 min. The citric acid act as an oxidant as well as a metal-binding agent in the reaction. The resultant metal-citrate complex was further added with ethylene glycol (two times that of the total amount of cations). It was heated at 90 °C for 1 h to facilitate the polymeric framework formation. Subsequently, the temperature was further increased to 120 °C that advances the transformation of the solution into a polymeric resinous state. The obtained dry white resin was charred at 400 °C in the air for 3 h to form a black fluffy mass. The charred material underwent calcination at 800 °C for 8 h. The resultant solid calcined aggregates were ground in pestle mortar into fine white powder and stored in a dry container for future adsorption experiments.

2.4. Characterization of the adsorbent

The assessment of the surface functional group of the synthesized sample was determined using an FT-IR spectrophotometer (FTLA-2000 ABB, Canada), and the spectra were recorded in the range of 4000–500 cm^{-1}. For crystallographic identification and phase purity assessment, the X-ray diffraction pattern of the sample was investigated. The same analysis was performed on Rigaku mini flex benchtop XRD recorded over a range of 10°–90° 2θ using radiation source Cu-Kα (λ = 0.154 nm). The interpretation of the surface morphology of the sample was carried out using a Scanning Electron Microscope (Zeiss, Germany) operated at an accelerated voltage of 5.0 kV. The synthesized particles were also investigated through Transmission Electron Spectroscopy of Hitachi (H-7500) operated at an accelerating voltage of 100 kV with a magnification up to 0.36 nm point to point resolution and 0.1 nm lattice resolution. The determination of the specific surface area of the synthesized material was conducted through a BET surface area analyser (ASAP 2020, Micromeritics).

3. Adsorption and photocatalytic studies

Batch experiments were carried out to investigate the adsorption competency of the synthesized perovskite sample. The adsorption process was optimized by varying the experimental conditions such as solution pH, adsorbent dose, contact time, and reaction temperature. In the present investigation, an optimized adsorbent dose of 0.4 g/L were used for all adsorption experiments. The pH of the solutions was maintained using 0.1 N HCl and 0.1 M NaOH. For experiments, different initial dye concentrations (10–200 mg/L) of fixed volume (100 mL) were taken in an Erlenmeyer flask and was added with an optimized adsorbent dose. The mixture was kept for agitation at 30 °C in a temperature-controlled water bath shaker (Narang Scientific Ltd., New Delhi, India) for a fixed time. Residual dye concentration in the solution was measured after fixed time intervals (5 min) using a double beam spectrophotometer (Systronics 2203, Ahmedabad, India) at a wavelength of λ_{max425} nm. Dye percentage removal and equilibrium adsorption capacity of the synthesized perovskite was calculated by following expressions:

$$\text{Dye removal}\,(\%) = \left(C_0 - C_e\right) \times \left(\frac{1}{C_0}\right) \times 100 \tag{1}$$

$$\text{Equilibrium adsorption capacity}\,\left(mgg^{-1}\right) q_e = \frac{C_0 - C_e}{M} \times V \tag{2}$$

C_0 and C_e represent the initial and equilibrium concentrations of dye; correspondingly, M denotes the mass of adsorbent (g), and V is the volume of solution. To avoid discrepancy and ambiguity, all sorption experiments were carried out three times with an error ≤5%. Experiments were re-performed in case deviations of greater than 5% were obtained.

For photocatalytic experiments, the reaction suspensions were arranged using 50 mL of dye solution containing a catalyst dose of 0.03 g taking initial dye concentrations of 10–100 mg/L. The experiments were performed in July, and the intensity of solar radiation was measured using a pyrheliometer each day before starting the experiments. On clear days the average intensity was measured as 910 $W/m^{2,}$ while on cloudy days, the intensity drops down to 330 W/m^2 on an average. Therefore, to achieve maximum efficiency, only sunny days were selected for conducting experiments. The investigation of photocatalytic performance was carried out by exposing the catalyst loaded dye solution in direct sunlight for an optimized time of 5 h under constant stirring conditions. The samples were periodically collected at definite time intervals and

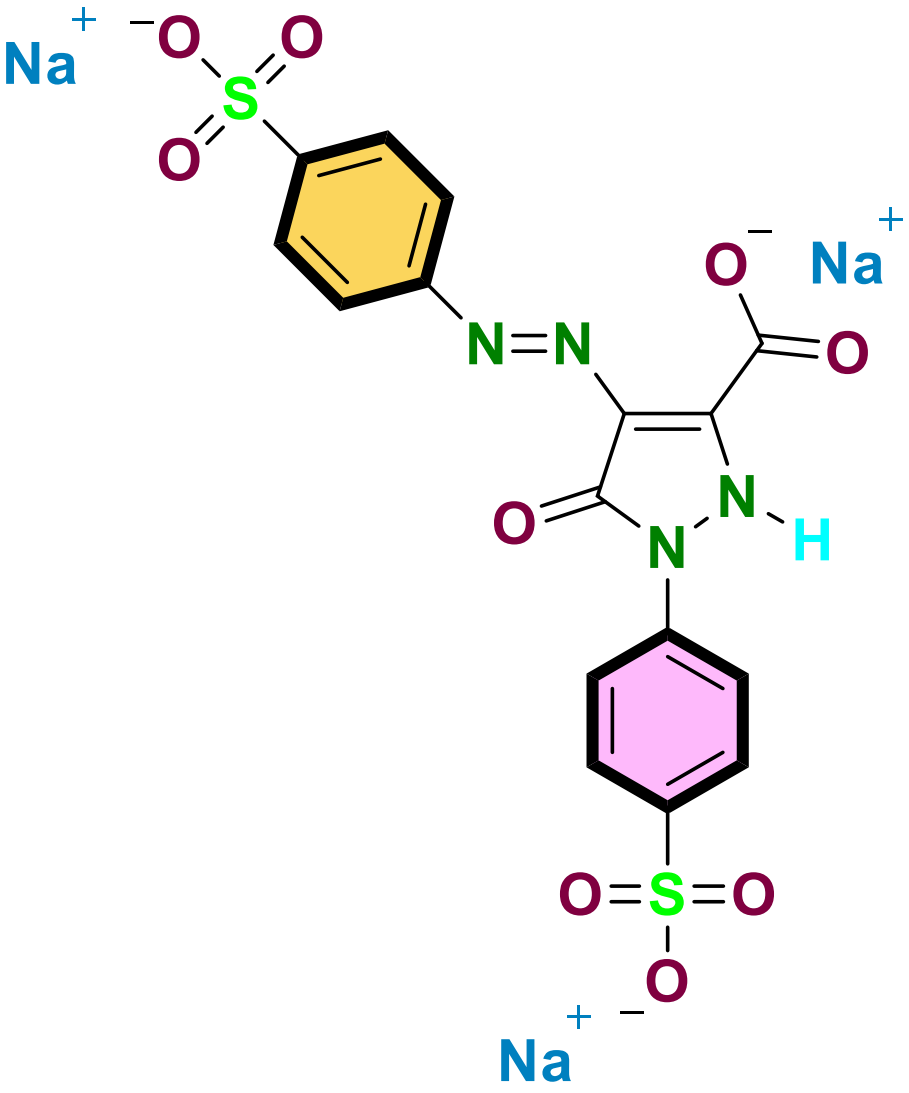

Fig. 1. Molecular structure of FD&C Yellow 5 (For interpretation of the references to color in this figure legend, the reader is referred to the web version of this article.).

were subjected to spectrophotometric measurements. However, before exposing the system to light reaction, the dye solution loaded with perovskite particles was agitated in the dark for 40 min to ensure adsorptive uptake of the adsorbate species over the solid catalyst surface. The photocatalytic efficiency of the synthesized perovskite can be quantified by using the following relation:

$$\eta = \frac{(1 - C_t)}{C_0} \times 100 \quad (3)$$

where C_t represent the remaining dye concentration at time t after photoreaction and C_0 is the initial dye concentration.

4. Results and discussion

4.1. Characterization of the adsorbent sample

Fig. 2a represents the FT-IR spectra for the pristine perovskite sample and dye loaded perovskite. The fresh sample exhibits a slight peak at around 3475 cm^{-1}, representing stretching of –OH group of water. However, this peak is not expected, as the sample is calcined at a high temperature of 800 °C which is supposed to eliminate the water content present in the sample. The unexpected peak may be due to the intrusion of moisture in the sample, which occurs maybe during sample analysis. The prominent peak at around 580 cm^{-1} is attributed to M-O (metal oxide) bond (Busca, 2009). The presence of only one peak at 580 cm^{-1} indicates that the sample comprise of bimetal oxide as a major component than parent oxides. If parent oxides are in large proportion, then two adsorption bands correspond to CeO_2 and La_2O_3 at around 550 cm^{-1} and 653 cm^{-1}, respectively, should be observed in the spectra (Bilel et al., 2020). But the peak at 580 cm^{-1} indicated that both parent oxide interacts with each other at high temperature to form a bimetal oxide. As a result, only one peak is observed between the characteristic absorption bands of parental oxides. The dye loaded spectra reveal several new peaks that indicate the interaction between the dye and the perovskite particles (compared with the FT-IR spectra of pure dye extracted from the Spectral Database for Organic Compounds SDBS No. 3109).

The synthesized sample's lattice parameters and phase structure were interpreted from the X-ray diffraction patterns given in Fig. 2b. The pattern reflects five prominent peaks with 2θ values at 28.9°, 32.8°, 47.2°, 55.4°, 57.6° with corresponding *hkl* values of (111), (200), (220), (311) and (222), indicating the formation $La_2Ce_2O_7$ phase having cubic fluorite type structure with space group Fm3m and compliance with JCPDS file no. 04-012-6396 (Zhang et al., 2016; Kishor Kumar and Kalathi, 2018). The absence of any other prominent peaks indicating phase purity of the synthesized samples. A similar pattern for $La_2Ce_2O_7$ perovskite particles was reported by Jung and Park (2015). The average crystallite size of the perovskite sample was calculated using Scherrer's

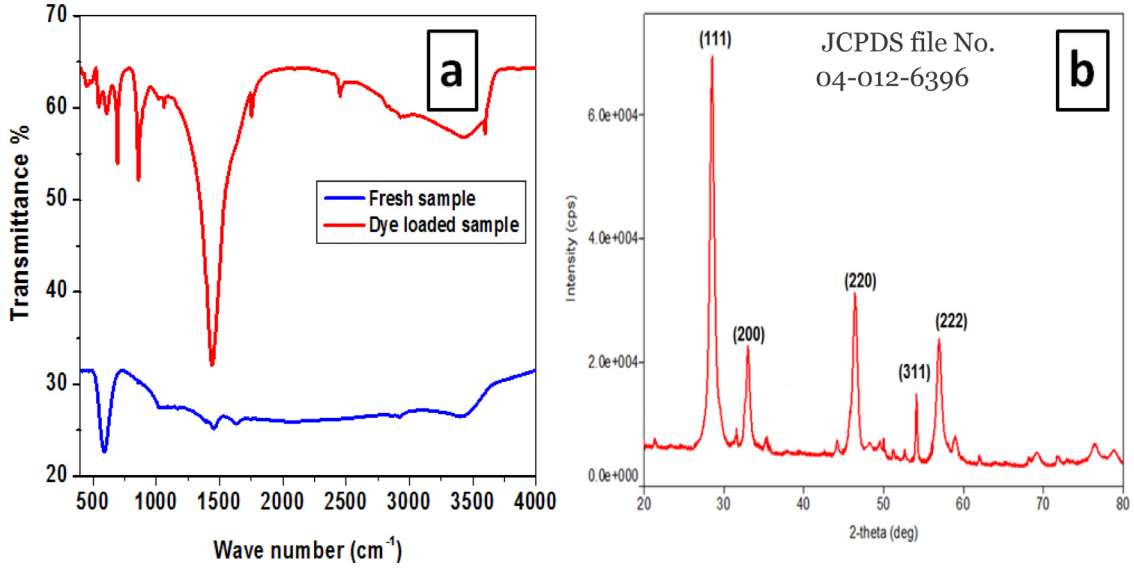

Fig. 2. (a) FTIR spectra for the fresh perovskite sample and dye loaded perovskite; (b) XRD diffractogram of perovskite sample.

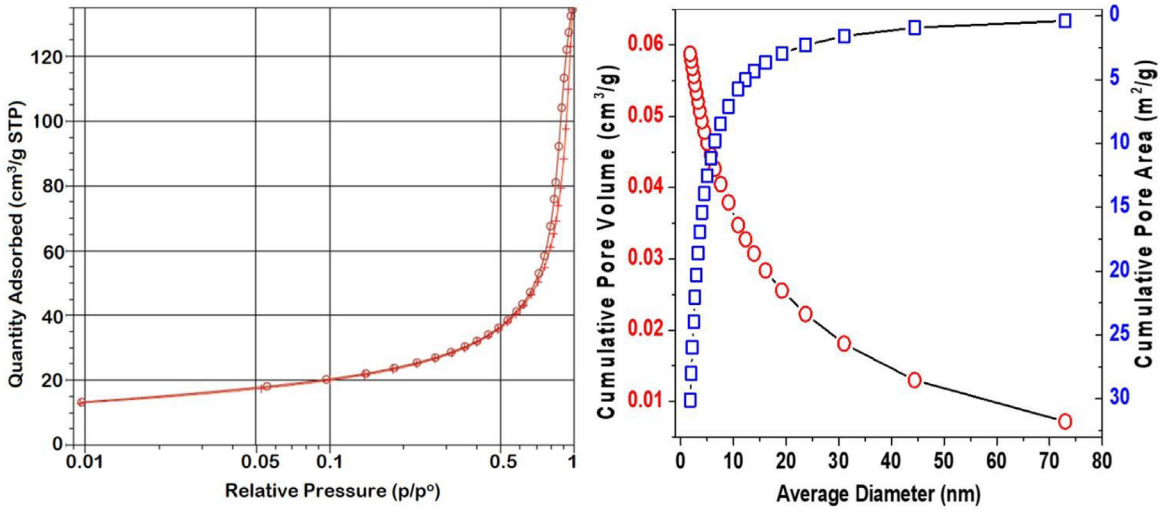

Fig. 3. (a) N_2 adsorption-desorption profile $La_2Ce_2O_7$ perovskite particles; (b) BJH pore volume and pore area.

relation (Jacob et al., 2014), given below:

$$D_{hkl} = k\lambda/\beta \cos\theta \quad (4)$$

where D is the crystallite size, k is the Scherrer constant (0.9), and λ represents X-ray diffraction wavelength (0.154 nm), and β is the full-width half maximum of the peaks. The average crystallite size of the material was calculated by considering five major peaks and was estimated to be ca. 64 nm.

The specific surface area of the $La_2Ce_2O_7$ perovskite particles was analysed through the N_2 adsorption-desorption profile (Fig. 3a). The profile seems to follow a type IV kind of adsorption isotherm and hysteresis loop curve as well. The resultant shape of the profile suggests some specific features such as the presence of narrow slit-like pores and irregularly shaped voids inside the pores and ordered internal arrangements of the pores. The BET surface of the sample was quantified as 64 m^2/g, which represents a moderate surface area that facilitates the effective interaction of the dye molecules with the reactive sites. The porosity of the sample was also estimated from BJH desorption pore distribution curves (Fig. 3b). The average pore diameter of the sample was found to be 11 nm indicating mesoporous nature, while the average cumulative pore area and cumulative pore volume were estimated to be 32 m^2/g and 0.061 cm^3/g, respectively.

The examination of the surface morphology of the synthesized perovskite particles was carried out *via* SEM analysis (Fig. 4a–c) at different magnifications. The particles were found to be plate-like flaky structure and irregular in shape. The closer view of the sample (Fig. 4c) depicted lots of smaller and bigger sized pores over the surface, giving it a porous sponge-like appearance. Thus, the SEM result demonstrates that the synthesized material is highly porous, which is also evident from the BJH analysis.

TEM analysis of the synthesized perovskite sample was also conducted to determine the size of the particle. Fig. 5a and b demonstrate TEM images of the particles from a different angle at a magnification of 176,000 X. The obtained image indicated that the synthesized material existed in a highly agglomerated state. Most of the particles seem to be overlapped, due to which the exact shape of the particle is not perfectly discernable. The size range of the synthesized particles was estimated using Image J software, and the particle size was found to exist within the range of 10–90 nm (Fig. 5c), out of which the particles of size range 60–70 nm are the most dominating.

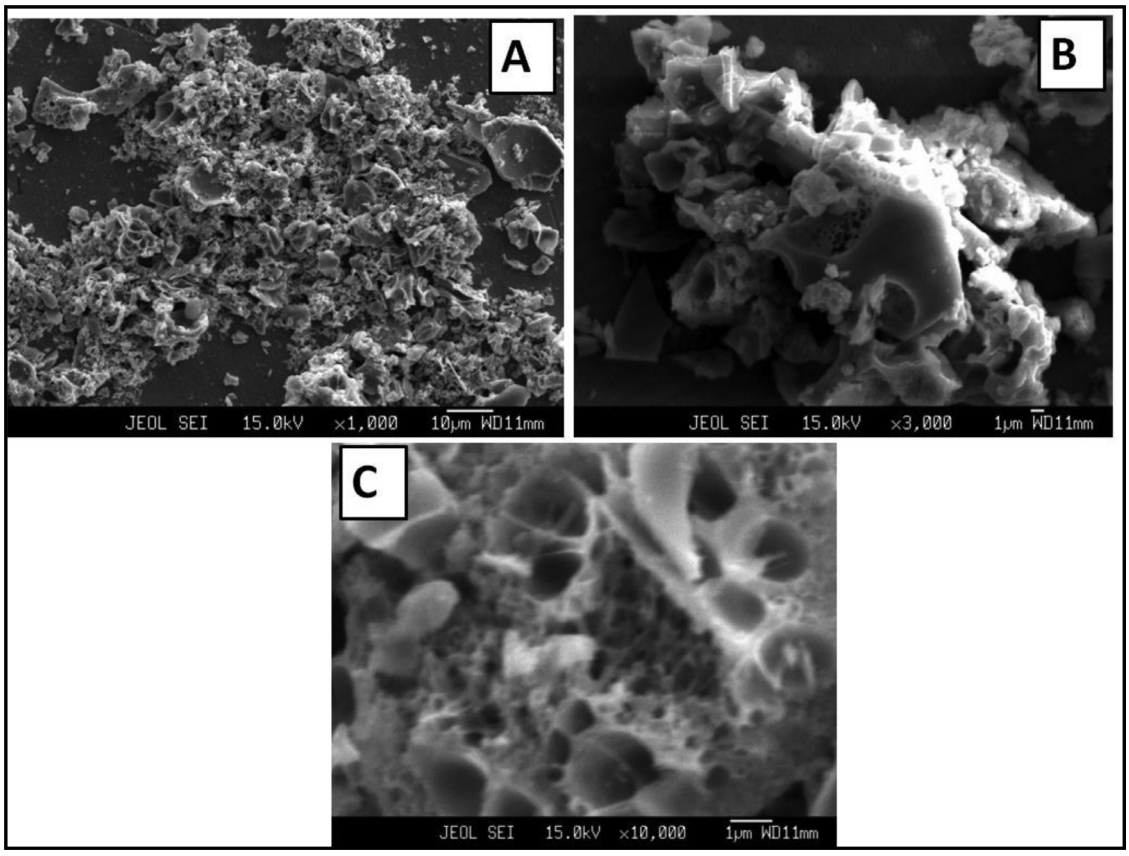

Fig. 4. 4a, 4b, 4c SEM analysis synthesized perovskite particles at different magnification.

4.2. Effect of solution pH

Solution pH plays a vital role in adsorption studies. Changing the solution pH is mainly responsible for structural modification of the adsorbate species or chemical amendment of the adsorbent species, influencing the overall adsorption behavior of the system. Fig. 6 demonstrate the dye removal performance of $La_2Ce_2O_7$ nanoparticles at varying solution pH conditions. The highest dye removal percent of 92% was achieved at pH 2.0. In contrast, the removal efficiency plummeted down to below 40% with an elevated pH value, suggesting that acidic condition favors rapid uptake of anionic adsorbate species. The pH-based removal mechanism can be explained through pH_{ZPC} analysis, representing the pH at which the adsorbent becomes electrically neutral. The pH_{ZPC} of the $La_2Ce_2O_7$ nanoparticles evaluated as 6.2, hence at pH <6.2 the adsorbent surface becomes highly protonated which facilitates binding of anionic species through electrostatic interaction while as the solution pH value increases beyond 6.2 the adsorbent surface starts deprotonating and discourages adsorption of dye species due to electrostatic repulsion (El-Bindary et al., 2018).

4.3. Adsorption kinetics

The interpretation of the interaction rate of the dye molecules with the $La_2Ce_2O_7$ perovskite nanoparticles can be scrutinized by treating the adsorption data as a function of time with various kinetics models. The evaluation of the kinetic data was carried out by employing two well-known and widely documented Lagergren's pseudo-first order and pseudo-second order (Moussout et al., 2018) kinetic models for the present adsorption system.

The linearized relations for Lagergren's pseudo-first order kinetics and pseudo-second order kinetics are given as follows:

$$\log\left(q_e - q_t\right) = \log q_e - \left(\frac{k_1}{2.303}\right).t \tag{5}$$

$$\frac{t}{q_t} = \frac{1}{k_2 q_e^{\,2}} + \frac{1}{t q_e} \tag{6}$$

where q_e is the amount of pollutant adsorbed at equilibrium time (mg/g), q_t, represents amount of pollutant adsorbed at time t (mg/g), k_1 is the pseudo-first order rate constant (min^{-1}) and k_2 corresponds to the pseudo-second order rate constant (g/mg/min).

The profile for pseudo-first order and pseudo-second order is depicted in Fig. 7a and b. The resultant relation of pseudo-first order seems to be found a little bit deviated at higher dye concentration while at lower concentration proper correlation is observed. In case of pseudo-second order the data points-maintained linearity for all concentrations and throughout the contact time. Moreover, the rate constant values estimated for the models found to be decreases gradually with increasing dye concentration, suggesting that due to low concentration of adsorbate species the interaction of the same with the reactive adsorbent sites took place rapidly; while with increasing concentration, the competition for the reactive sites between the dye molecules becomes exacerbated and thus limited the rate constant values of the reaction.

To interpret the suitability of the appropriate model, the R^2 values and statistical parameters *ERRSQ* and *MPSD* were taken into consideration. From the careful perusal of the results given in Table 1, it's demonstrated that the pseudo-second order kinetic model is relatively more appropriate than pseudo-first order model due to its high R^2 values and low statistical parametric values, indicating the aptness of the model in representing the rate constant data of the adsorption system more precisely.

The kinetic data was also investigated to understand the rate-controlling step of the adsorption interaction between food dye and $La_2Ce_2O_7$ perovskite nanoparticles. The elucidation of the mechanism of the adsorption reaction was expounded through the fitting of the experimental adsorption kinetics data in the intra-particle diffusion model

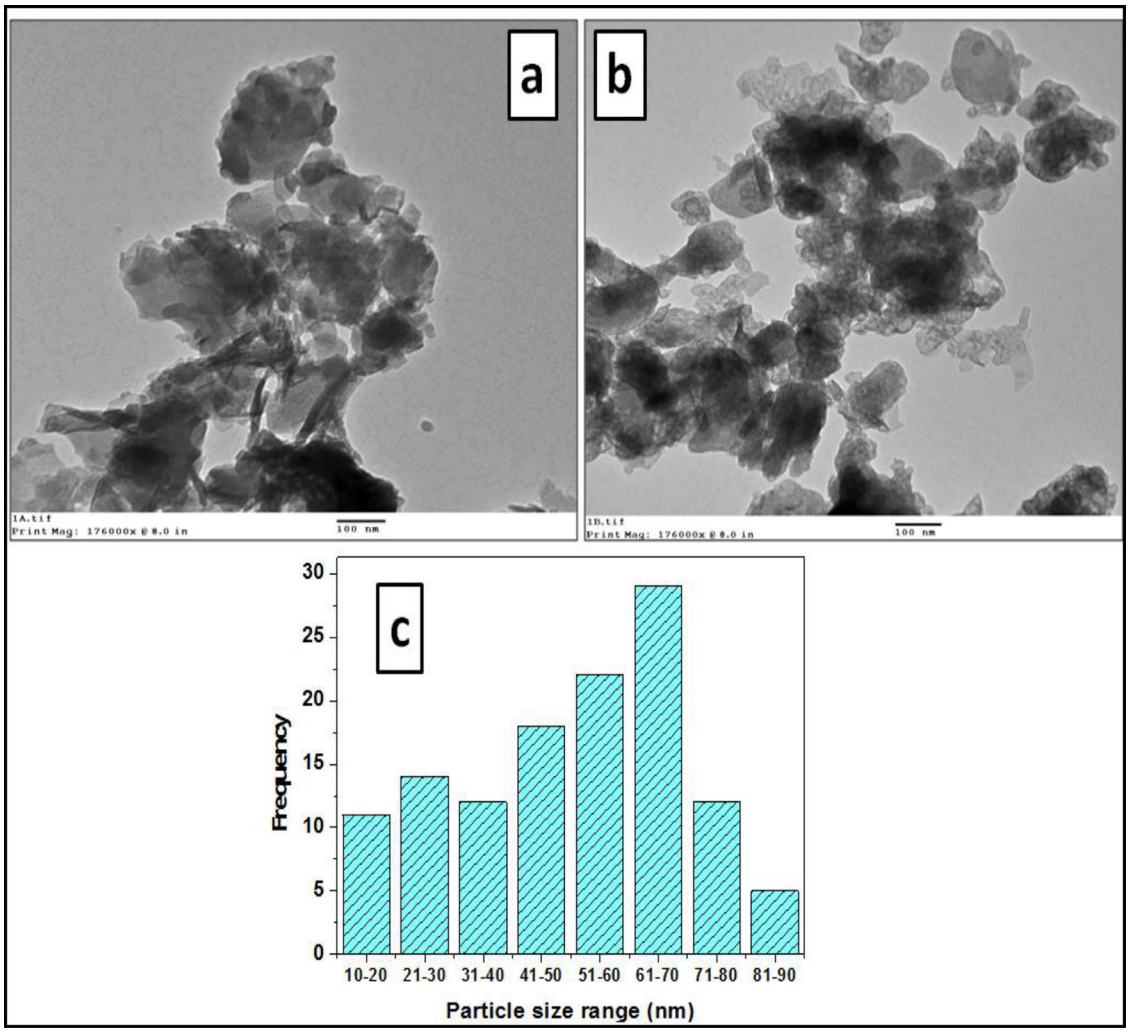

Fig. 5. 5a and 5b TEM image at different resolution; 5c particle size distribution analysis.

Table 1
Kinetic parameters calculated for Food dye adsorption on to lanthanum cerate nanoparticles.

Pseudo-first-order	10 mg L^{-1}	25 mg L^{-1}	50 mg L^{-1}	100 mg L^{-1}	200 mg L^{-1}
k_1 x10^{-2} (min^{-1})	4.72	4.43	4.23	4.17	3.98
$q_{e(cal)}$ (mg g^{-1})	25.11	61.23	91.22	125.89	251.1
$q_{e(exp)}$ (mg g^{-1})	23.57	57.92	89.41	188.01	321.6
R^2	0.980	0.996	0.976	0.981	0.963
ERRSQ	2.37	10.95	3.27	3969	4900
NSD%	14.75	13.80	8.21	33.16	27.03

Pseudo-second-order	10 mg L^{-1}	25 mg L^{-1}	50 mg L^{-1}	100 mg L^{-1}	200 mg L^{-1}
$k_2 \times 10^{-3}$ ($gmin^{-1}mg^{-1}$)	3.74	2.14	1.33	0.78	0.34
$q_{e\ (cal)}$ (mg g^{-1})	26.95	54.91	106.27	191.9	337.8
R^2	0.992	0.995	0.991	0.988	0.986
ERRSQ	11.42	9.06	284.2	15.13	262.4
NSD%	21.86	13.16	25.07	8.30	12.95

Intra-particle diffusion	10 mg L^{-1}	25 mg L^{-1}	50 mg L^{-1}	100 mg L^{-1}	200 mg L^{-1}
$k_{id,Film}$ ($mgg^{-1}min^{-0.5}$)	1.05	1.23	1.41	1.83	2.14
C_1	4.11	10.56	19.72	37.46	61.79
R^2	0.996	0.997	0.997	0.997	0.996
$k_{id,pore}$ ($mgg^{-1}min^{-0.5}$)	1.26	2.64	3.28	4.45	5.22
C_2	10.22	38.08	60.44	74.1	93.11
R^2	0.995	0.999	0.986	0.997	0.999

Mass Transfer Model	10 mg L^{-1}	25 mg L^{-1}	50 mg L^{-1}	100 mg L^{-1}	200 mg L^{-1}
β_L x 10^{-7} (cm s^{-1})	1.22	1.27	1.44	1.56	1.69

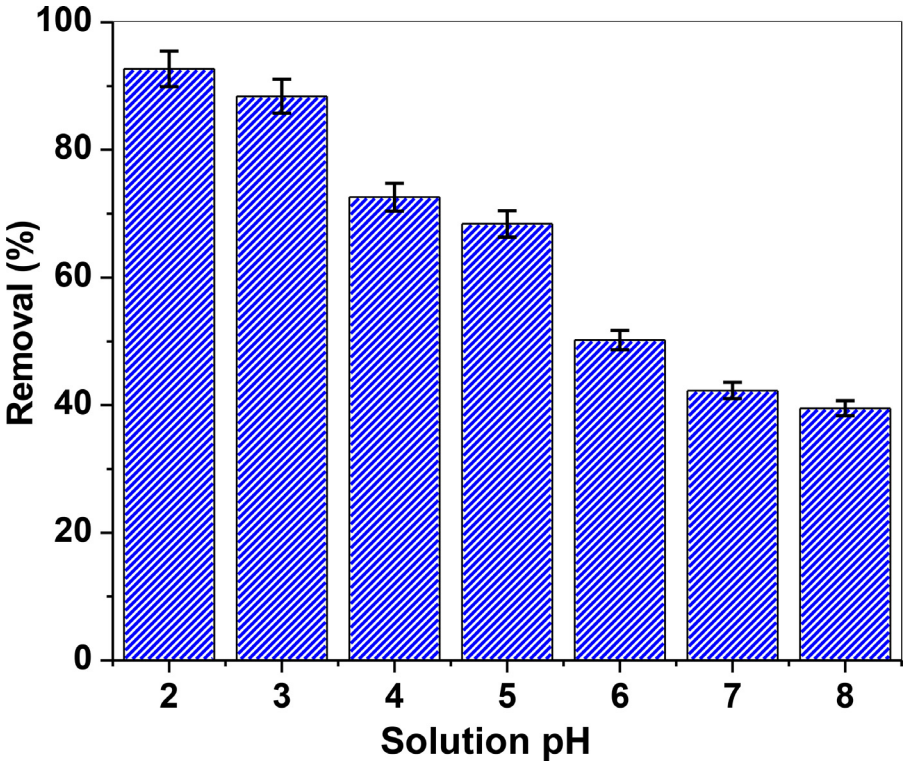

Fig 6. Dye removal performance of $La_2Ce_2O_7$ nanoparticles at varying solution pH condition (Initial dye conc. 25 mg/L; solution temp. 30 °C; adsorbent dose; 0.4 g/L).

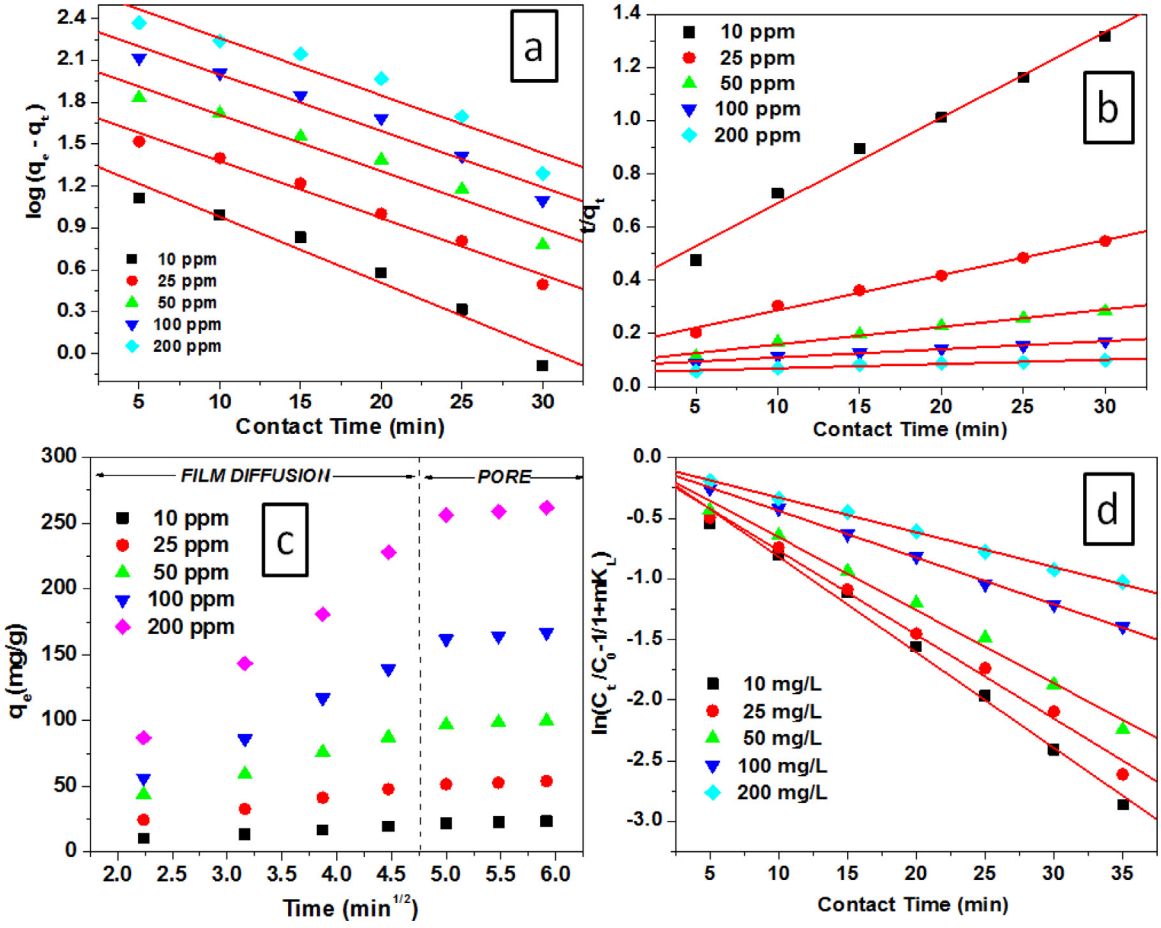

Fig. 7. (a) Kinetics pseudo first order plots; (b) kinetics pseudo second order plots; (c) intra-particle diffusion plots; (d) Mass transfer plots for the adsorption of food dye on perovskite particles.

given by Weber and Morris (1963) provided as below:

$$q_t = k_{id} t^{0.5} + C \quad (7)$$

where, q_t is the amount of pollutant adsorbed at time t (mg/g), k_{id} and C represents Intra-particle diffusion constant (mg/g $min^{0.5}$) and thickness of the transition layer (mg/g), respectively.

Fig. 7c depicted the curve obtained for the intra-particle diffusion model. The resultant curve reflects two prominent demarcated region, the first region corresponds to film diffusion process which represents the interaction of the dye with the active surface sites of the perovskite nanoparticles and the second region represented the pore diffusion phenomenon indicating the transmigration of the pollutants from the surface into the pores of the adsorbent. The first process is a relatively fast process that can be further correlated with the high-rate constant ($k_{id,\ film}$) values and low thickness (C_{film}) values of the transition layer obtained at an initial contact time. However, as the adsorption process proceed and contact time increases, the diffusion process comes into play which is marked by sluggish and impeded interaction of adsorbate species with the internal pore space of the adsorbent. The decrease in rate constant values ($k_{id,\ pore}$) was obtained to support the above process. Nevertheless, it can be observed that more than 50% of the removal was achieved within 20 min of the contact time, which is dominated by the film diffusion process. Overall, it can be concluded that the ongoing reaction mechanism found to be governed by the film diffusion process, and also the rate-limiting step of the dye and perovskite interaction can be better interpreted through the film diffusion mechanism.

4.4. Mass transfer investigation

The interpretation of the transmigration behavior of the contaminants from the liquid bulk phase to the solid surface of the adsorbent can be understood and quantified through the mass transfer model. During the adsorption process, the unsaturated reactive sites present on the adsorbent surface allow contaminants present in the bulk liquid solution to interact with the former either electrostatically or chemically. But this process profoundly governs the mass transfer resistance, which comes into play when contaminants from the liquid medium try to drift towards the solid adsorbent surface. This solid-liquid interface offers resistance to the contaminants, which as a result, impede the adsorption process. Hence, through mass transfer analysis, the transportation rate of the contaminants from the liquid phase over to the solid surface can be numerically appraised. The results help ascertain the efficiency of the treatment process. For mass transfer analysis, experimentally acquired kinetic data was treated with a mathematical expression given by McKay and Poots (1980) is represented as follows:

$$\ln\{(C_t/C_0 - 1)/(1 + mk)\} = \ln\{(mk/(1 + mk) - (1 + mk)/mk)\}\ \beta_L S_s.t \quad (8)$$

where C_o is the initial concentration of the adsorbate (mg/L) and C_t symbolizes concentration of adsorbate after time 't' (mg/L); k represents the product of Langmuir adsorption capacity Q_{max} and energy parameter b; β_L corresponds to mass transfer coefficient, cm/s; and m identified as the mass of the adsorbent per unit volume of the dye solution (g/L) and is given by

$$m = M/V \quad (9)$$

S_s is the specific surface area of the adsorbent (m^2/g) and is calculated as:

$$S_s = 6\ m/(d_p \rho_p\ (1 - \in_p)) \quad (10)$$

where d_p indicates particle diameter (cm) taken as 64 nm; ρ_p represents the bulk density of the adsorbent (g/cm^3) estimated as 5.0 g/cm^3, and ϵ_p refers to the porosity of the adsorbent particles, which is evaluated as 0.6. The values of the mass transfer coefficient (β_L) were determined from the slopes of the linear plot of ln [(C_t /C_0) – 1/(1+mk)] versus t. The plotted mass transfer profile (Fig. 7d) demonstrate straight lines and good linearity. The mass transfer values for five specified concentrations were evaluated and provided in Table 1. The calculated mass transfer values demonstrate an increasing trend with increasing concentration, which indicates the availability of potential active sites over the adsorbent surface. These active sites permit many dye molecules to overcome the mass transfer barrier more effectively. The magnitude of electrostatic pull exerted by the active surface sites is relatively much higher when many dye molecules are available. While with decreasing dye concentration, the Coulombic pull exerted by the sites becomes relatively weaker; hence overall mass transfer rate also declines.

4.5. Adsorption isotherm

The mechanism of adsorption, as a function of concentration at a fixed temperature, can be consummated through the investigation of adsorption isotherm. The study helps in the determination of the adsorption capacity of the adsorbent. Also, it gives an idea about the nature of the interaction between the adsorbate species and adsorbent. The quantitative and qualitative estimation of the aforementioned parameters can be executed by fitting the experimentally obtained adsorption data into adsorption isotherm models. The study was accomplished by employing Langmuir, Freundlich, Dubinin-Radushkevich, and Temkin adsorption isotherm models into the experimentally obtained adsorption data.

Langmuir model (Jeppu and Clement, 2012) demonstrates the monolayered interaction of adsorbate molecules with adsorbent surfaces having limited active sites, and no lateral interaction is possible between the adsorbate molecules. The linear expression of the model is represented as:

$$\frac{C_e}{q_e} = \frac{1}{Q_{max} b} + \frac{C_e}{Q_{max}} \quad (11)$$

where q_e is the quantity of dye sorbed (mg/g) at equilibrium and C_e is the equilibrium liquid-phase residual concentrations of dye (mg/L), and b is the Langmuir constant (L/mg) indicating apparent energy of sorption, Q_{max} is the maximum adsorption capacity (mg/g).

The resultant plot of C_e/q_e versus C_e (Fig. 8a) exhibit moderate deviation from the linearity with relatively low R^2 values and high error values, suggesting the inapplicability of the model in describing the food dye and perovskite nanoparticles based sorption system.

Further, the parameter of the Langmuir model can also be used for interpreting the adsorption behavior of the dye-perovskite nanoparticles system by estimating the 'separation factor R_L' using the following relation:

$$R_L = \frac{1}{1 + b\ C_O} \quad (12)$$

where C_0 is the initial concentration of adsorbate (mg/L). The irreversibility (R_L= 0), linearity (R_L=1) and viability (0 <R_L< 1) of the sorption process is determined by the values of R_L. In the present work, the values of R_L were in the range of 0,1, attesting the adsorption of dye over $La_2Ce_2O_7$ nanoparticles is highly favorable.

For the interpretation of the heterogeneous adsorption system, the resultant sorption data were fitted to the Freundlich model (Jeppu and Clement, 2012). The model suggests a heterogeneous reaction of the adsorbate molecules with the adsorbent surface and forming a multilayer coverage over the surface of adsorbent through lateral interaction between the adsorbate. Linearized representation of the model provided as:

$$\ln q_e = \ln K_F + \frac{1}{n} \ln C_e \quad (13)$$

where K_F and n are the coefficients related to adsorption capacity and adsorption intensity, respectively. These coefficients were evaluated from the graph plotted between ln q_e versus ln C_e over the investigated temperature range. The profile (Fig. 8b) obtained displayed reasonable

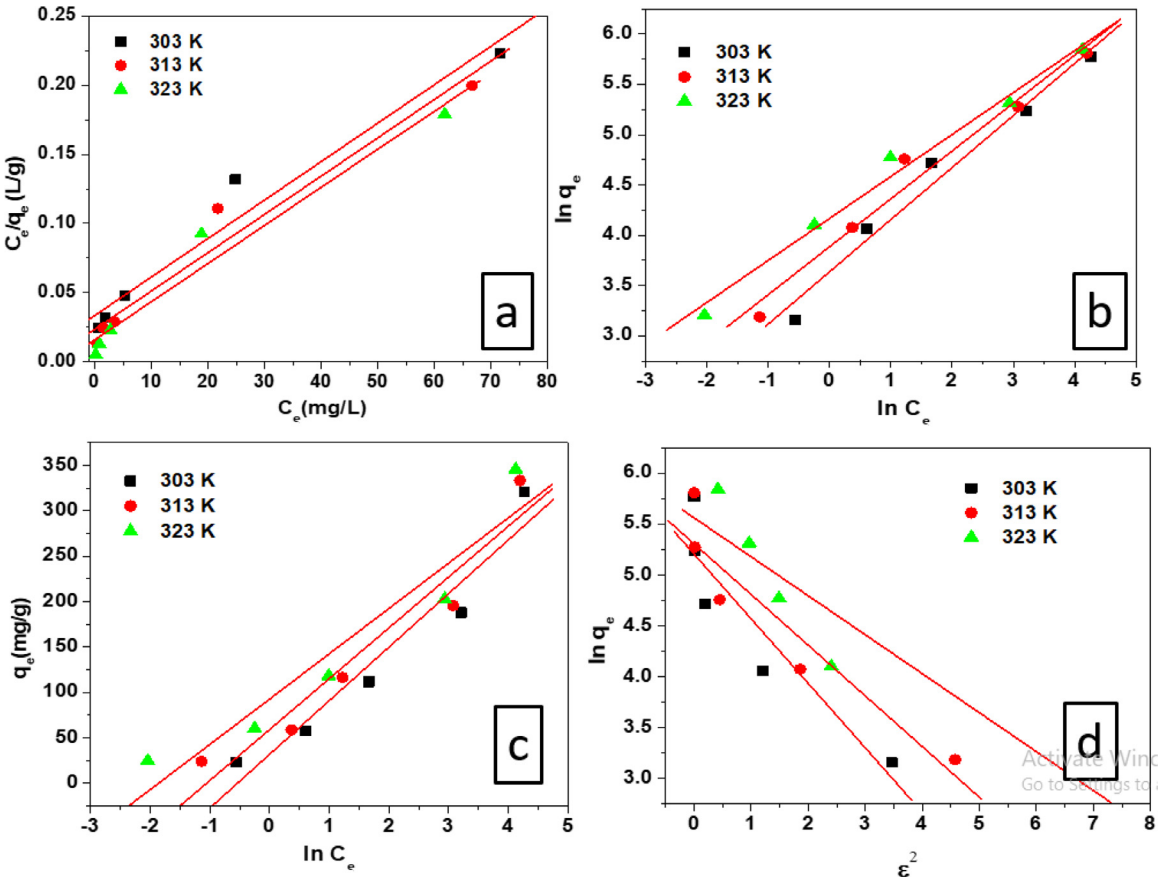

Fig. 8. (a) Langmuir isotherm plots; (b) Freundlich isotherm plots; isotherm plots; (c) Temkin isotherm plots; (d) Dubinin-Radushkevich .

linearity with relatively high R^2 values low error values, strongly advocating the relevance of the model in describing the dye-perovskite adsorption system. The values of n were found to be approaches to zero with increasing temperature suggesting surface heterogeneity enhances with solution temperature; as a result, K_F also observed to increase with temperature suggesting elevated temperature favors adsorption of the dye molecule.

Temkin model (Langmuir, 2012) assumes that the energy of the sorption process decreases linearly as coverage of the adsorbent surface with adsorbate molecules proceed gradually. The linear equation of the model is expressed as:

$$q_e = B \ln K_T + B \ln C_e \tag{14a}$$

$$B = \frac{RT}{b} \tag{14b}$$

where B is the Temkin constant signifies heat of adsorption, K_T is the Temkin equilibrium binding constant represents maximum binding energy (L/mg). The isotherm constants K_T and B were deduced from the linear plot of q_e versus ln C_e. The fitting lines (Fig. 8c) intensely diverge from the linearity, suggesting that the model is inappropriate for the present adsorption system.

D-R isotherm (Hutson and Yang, 1997) conceptualized the influence of the adsorbent porosity on the adsorption process, and its parameter also gives an idea about the nature of the adsorption process. The D-R equation in its linear form is given below:

$$\ln q_e = \ln q_m - \beta\varepsilon^2 \tag{15}$$

where q_e denotes the quantity of adsorbate species adsorbed per unit adsorbent dose (mg/g), q_m is the theoretical monolayer saturation capacity (mg/g), β represents activity coefficient (mol^2/kJ^2) to quantify the mean adsorption energy, ε is the Polyani potential which can be obtained from the following equation:

$$\varepsilon = RT\ ln\left[1 + \left(\frac{1}{C_e}\right)\right] \tag{16}$$

where R denotes the gas constant (0.008314 kJ/mol/K), T is the absolute temperature in Kelvin. C_e defined previously. The values of D-R isotherm constant E and q_m were evaluated from the slope and the intercept of the linear plot of ln q_e and ε^2 (Fig. 8d). The resultant plots reveal compromised linearity and lower values of R^2, indicating the limited scope of the D-R model in explaining the sorption process. However, the model can be used to ascertain the nature of the adsorption process by quantification of E parameter using relation given as below.

$$E = \frac{1}{\sqrt{2\beta}} \tag{17}$$

If the parametric value of E lies between 8 and 16 kJ/mol, the adsorption process is said to follow the chemisorption mechanism, while a value less than 8 kJ/mol, indicates the dominancy of the physisorption process. All the E values were examined and found to be less than 8 kJ/mol, implying that physical forces govern the adsorption of dye species onto $La_2Ce_2O_7$ nanoparticles. Moreover, the fitting of adsorption data to the second-order kinetic model also indicates the chemisorption process's involvement. So, overall it can be stated that the entire interaction process was found to be majorly controlled by the physisorption mechanism with some chemisorption contribution.

The parametric values for all isotherm models and the error values were calculated and depicted in Table 2. Comparison of the adsorption capacities and experimental conditions investigated by the researchers for the adsorption of food dye FD&C Yellow 5 on a different class of adsorbent materials (Ebrahimpoor et al., 2021; Ouassif et al., 2020; Chukwuemeka-Okorie et al., 2021; Reck et al., 2018; Gautam et al.,

Table 2
Various adsorption isotherm parameters calculated for the adsorption of Food dye FD&C Yellow 5 dye on lanthanum cerate nanoparticles.

Dye	Model	30 °C	40 °C	50 °C
FD&C Yellow 5	Langmuir			
	Q_{max}(mgg^{-1})	138.3	140.4	141.6
	b(L/mg)	0.219	0.304	0.438
	R_L Range	0.313–0.022	0.247–0.016	0.185–0.011
	R^2	0.983	0.986	0.981
	ERRSQ	1.4	0.63	0.59
	NSD%	0.24	1.31	1.04
	Freundlich			
	K_F(mg g^{-1})(L mg^{-1})$^{1/n}$	114.8	128.6	133.3
	n	1.93	2.11	2.39
	R^2	0.991	0.988	0.996
	ERRSQ	0.32	0.29	0.39
	NSD%	2.24	2.56	1.29
	Dubinin- Radushkevich			
	q_m (mg g^{-1})	160.5	203.2	229.1
	β (mol^2 kJ^{-2})	0.102	0.098	0.082
	E (kJ mol^{-1})	2.21	2.24	2.47
	R^2	0.921	0.953	0.928
	ERRSQ	0.76	0.59	0.88
	NSD%	3.31	2.02	7.11
	Tempkin			
	B	49.4	52.6	56.1
	A	4.46	5.01	5.75
	b	0.0514	0.0502	0.0479
	R^2	0.967	0.964	0.956
	ERRSQ	0.85	0.92	0.54
	NSD%	4.54	7.73	6.72

2019; Sahnoun et al., 2018; Banerjee and Chattopadhyaya, 2017; Goscianska and Pietrzak, 2014; Klett et al., 2014; Srivastava et al., 2015) are listed in Table 3. From the table, it is evident that the experimental conditions contributed a substantial role in modifying the adsorption capacity of the sorbent species.

4.6. Thermodynamics and activation energy

Temperature plays a vital role in governing the adsorption process. The molecules behave differently at various temperatures due to the change in viscosity flow, which enhances the escaping tendency of the fluid in the form of vapour into the atmosphere. In response to this, molecules present in the bulk phase also reacts by changing their orientation or mobility. Hence, the response of contaminants as a function of temperature can be interpreted by measuring specific parameters like standard Gibb's free energy (ΔG^o), enthalpy (ΔH^o), and entropy (ΔS^o) by plotting profiles using models (Ahmad et al., 2014) provided below:

$$\log b = \left(\frac{\Delta S^o}{2.303R}\right) - \left(\frac{\Delta H^o}{2.303RT}\right) \quad (18)$$

$$\Delta G^o = \Delta H^o - T\Delta S^o \quad (19)$$

where b denote Langmuir constant, and R is the gas constant value (8.314 J/mol K) and T is the absolute temperature in Kelvin. The thermodynamic parameters ΔH^o and ΔS^o were quantified using Eq. (18), and the obtained values were used to calculate $\Delta G^o$for three specified reaction temperatures. The values for ΔH^o and ΔS^o were estimated to be 3.28 kJ/mol and 0.013 kJ/mol K, respectively. The positive change in enthalpy values indicating that the dye sorption reaction is endothermic, and the interaction process favors high reaction temperature further positive ΔS^o the value indicates increasing randomness, which may be corroborated to the desorption of adsorbed water molecules from the adsorbent surface during dye adsorption. The sorption process was also found to be feasible and spontaneous as all the estimated ΔG^ovalues were found to be negative. The ΔG^ovalues were calculated as –0.749, –0.882, and –1.015 kJ/mol at 303 K, 313 K and 323 K, respectively.

The activation energy was also investigated for the sorption of food dye on perovskite nanoparticles using Arrhenius relation (Arrhenius, 1889) given below:

$$\ln k_2 = \ln A - \frac{Ea}{RT} \quad (20)$$

where k_2 represents the rate constant of pseudo second order kinetics, R refers to the universal gas constant (8.314 Jmol^{-1} K^{-1}), and T absolute temperature (K). Activation energy value can be determined from the slope of the linear plot of ln k_2 vs 1/T (Fig not shown), and the value was estimated to be 5.26 kJ/mol. The activation energy value gives an idea about the interaction behavior. For the chemisorption process, the activation energy value should always be greater than 40 kJ/mol, while a value less than this value indicates the physisorption process. Hence, the obtained activation energy values recommend that the present sorption system govern by physisorption interaction.

4.7. Regeneration and recycling study

The perovskite species' endurance capacity and recycling ability were investigated by performing desorption experiments using 50 mg/L of dye solution. To conduct the desorption reaction, 0.1 M of NaOH solution was used as an eluting reagent. The dye exhausted adsorbent of 0.04 g was treated with 100 mL of 0.1 M of NaOH solution and kept under stirring for 50 min (optimized time). After the completion of the desorption reaction, the resultant desorbed solution was spectrophotometrically tested and was analysed for residual dye concentration. The dye desorption was investigated as 98%. The plausible mechanism behind the dye desorption can be attributed to the replacement of negatively charged dye ions with $^-$OH ions of the eluent used. The adsorbent particles recovered from the desorption process were subjected to calcination at 500 °C for 6 h to restore the adsorbent activity. The calcined particles were then tested for their reusability. Similar adsorption-desorption runs, followed by a calcination process, and were performed until the uptake capacity of the adsorbent declined significantly. The dye removal percentage investigated for 0 to 9 regeneration cycles were 89.4%, 85.2%, 84%, 82.7%, 80.1%, 78.2%, 76.6%, 69.7%, and 54.3%, respectively. The results indicate that the adsorbent material can be efficiently reused up to six times without a substantial loss in the adsorbent's uptake efficacy.

4.8. Photocatalytic investigation

The most concerning part of the adsorption process lies in the fact that once the adsorbent material reached its endurance limit it was disposed off either by flushing the exhausted material out into the laboratory drains and finally end up to municipal sewage, or by scrapping out the material from the glassware into nearby garbage bins which ultimately end up to the landfills. These exhausted adsorbents were actually loaded with various toxic organic and inorganic species. With the change in surrounding pH conditions, the loaded adsorbent materials become highly susceptible to the desorption reaction that eventuates the immediate release of the adsorbed material back into the environment. However, this unintended release of the accumulated toxic species from the solid surface can be managed or controlled through chemical transformation of the organic molecules into less hazardous or nonhazardous products via photocatalysis mediated interaction. Fig. 9 demonstrates the photocatalytic performance of the synthesized $La_2Ce_2O_7$ perovskite nanoparticles, and the results suggest that the material is highly efficient in carrying out the degradation of the dye species. Overall, the photocatalytic activity comprise of three major steps that includes generation of active charge carriers (electrons/holes) when catalyst is exposed to strong sunlight followed by the redox reaction process that initiate between the adsorbed dye molecules and active charge carriers and finally desorption of the products from the solid surface of the catalyst (Chiu et al., 2019). A plausible mechanism (Soltani and Entezari, 2013)

Table 3
Comparison of the maximum monolayer adsorption of yellow 5 dye (Tartrazine) onto adsorbents from various sources.

Adsorbent	Experimental Conditions	Maximum adsorption capacity (mg/g)	References
$La_2Ce_2O_7$ perovskite particles	Adsorbent dose = 0.4 g/100 mL; Initial conc. (10–200 mg/L); pH = 2.0; time = 35 min; temperature = 323 K.	133.3	Present study
Polypyrrole/$SrFe_{12}O_{19}$/Graphene Oxide Nanocomposite	Adsorbent dose = 0.02 g/20 mL; Initial conc. (20–60 mg/L); pH = 6.5; time = 60 min; room temperature.	123.4	Ebrahimpoor et al. (2021)
Zn_2 AlCl-Layered Double Hydroxide	Adsorbent dose = 0.4 g/L; Initial conc. (10–240 mg/L); pH = 5.8; time = 60 min; temperature = 298 K.	282.48	Ouassif et al. (2020)
Activated carbon from cassava seivate	Adsorbent dose = 0.1 g/L; Initial conc. (30–150 mg/L); pH 1.0; time = 90 min; temperature = 40 °C.	20.83	Chukwuemeka-Okorie et al. (2021)
Moringa oleifera	Adsorbent dose = 0.2 g/50 mL; Initial conc. (5–70 mg/L); pH 3.0; time = 4 h; temperature = 15 °C.	91.27	Reck et al. (2018)
Iron nanoadsorbents	Adsorbent dose = 0.2 g/L, pH = 2.0, Initial conc. (25–100 mg/L); time = 90 min; temperature = 323 K.	68.78	Gautam et al. (2019)
Octadecyltrimethylammonium bromide-modified bentonite	Adsorbent dose = 10 mg/10 mL; Initial conc. (200 mg/L); pH = 2.0; time = 60 min; temperature = 22 °C.	201.0	Sahnoun et al. (2018)
Saw dust	Adsorbent dose = 5 g; Initial conc. (1–15 mg/L); pH 3.0; time = 70 min; temperature = 318 K.	4.71	Banerjee and Chattopadhyaya (2017)
Carbon nanotubes decorated with silver nanoparticles	Adsorbent dose = 25 mg/50 mL; Initial conc. (0–50 mg/L); pH= 3.0; time = 60 min.	84.04	Goscianska and Pietrzak (2014)
Nickel doped Zinc oxide	Adsorbent dose = 0.1 g/25 mL; Initial conc. (100–200 mg/L); pH 4.0, time = 10 min.	22.45	Klett et al. (2014)
Polypyrrole coated tenorite nanoparticles	Adsorbent dose = 3.3 g/L, pH 2.0, temperature = 45 °C, time = 300 min	42.50	Srivastava et al. (2015)

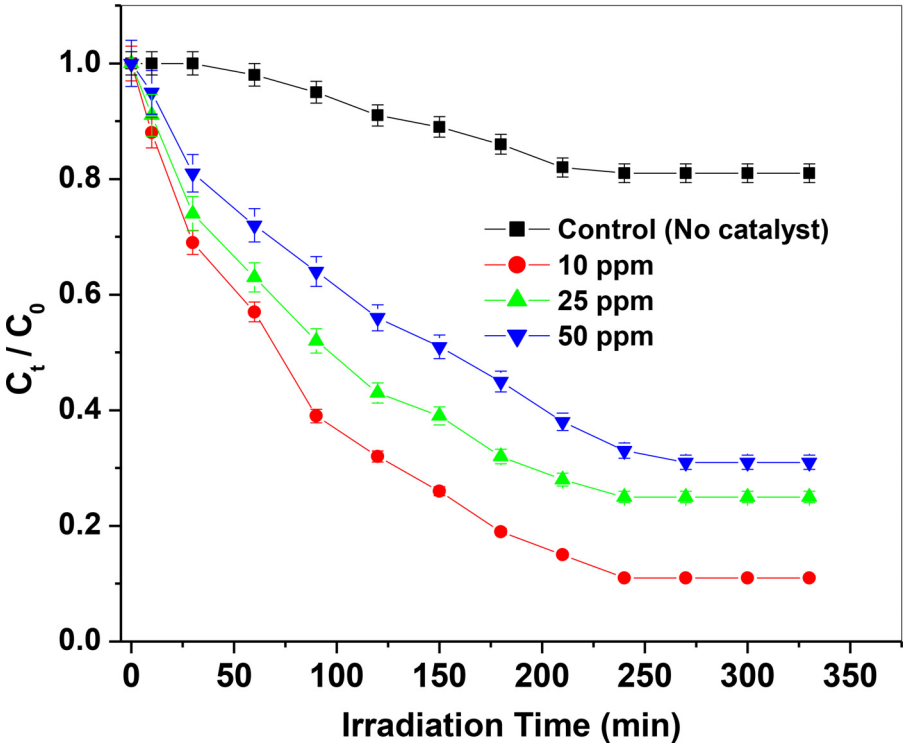

Fig. 9. Photocatalytic performance of the perovskite particles.

describing the photocatalytic degradation behavior of the $La_2Ce_2O_7$ perovskite particles is depicted in Fig. 10. Commendable photocatalytic performance has been observed for $La_2Ce_2O_7$ nanoparticles, mainly attributed to its high adsorption ability, enhanced surface area, and low bandgap energy. The high saturation capacity of 133.33 mg/g of perovskite particles indicates its intense surface affinity for dye molecules, allowing many dye molecules to be available for the redox reaction.

Further, the availability of enhanced surface area provides enormous active sites and facilitates adsorption of a large number of dye molecules, water and molecular oxygen. The molecular oxygen adsorbed by the perovskite particles captures photogenerated electrons to liberate active O_2^- species and is consequently responsible for the high photocatalytic activity. In addition to this high surface area and small particle size reduce the recombination rate of photogenerated charge carriers (e^-_{CB} and h^+_{VB} pairs) and maximize the escape of active e^-_{CB}/h^+_{VB} pairs from the surface.

Moreover, the energy bandgap also plays a significant role in the process. A low energy gap eases the movement of an electron from the valance band to the conduction band after absorbing a photon of light. Consequently, it creates an $e^-$and h^+ pair on the catalyst's surface and eventually produces highly reactive superoxide and hydroxy radicals that promote the degradation process. The bandgap of $La_2Ce_2O_7$ was

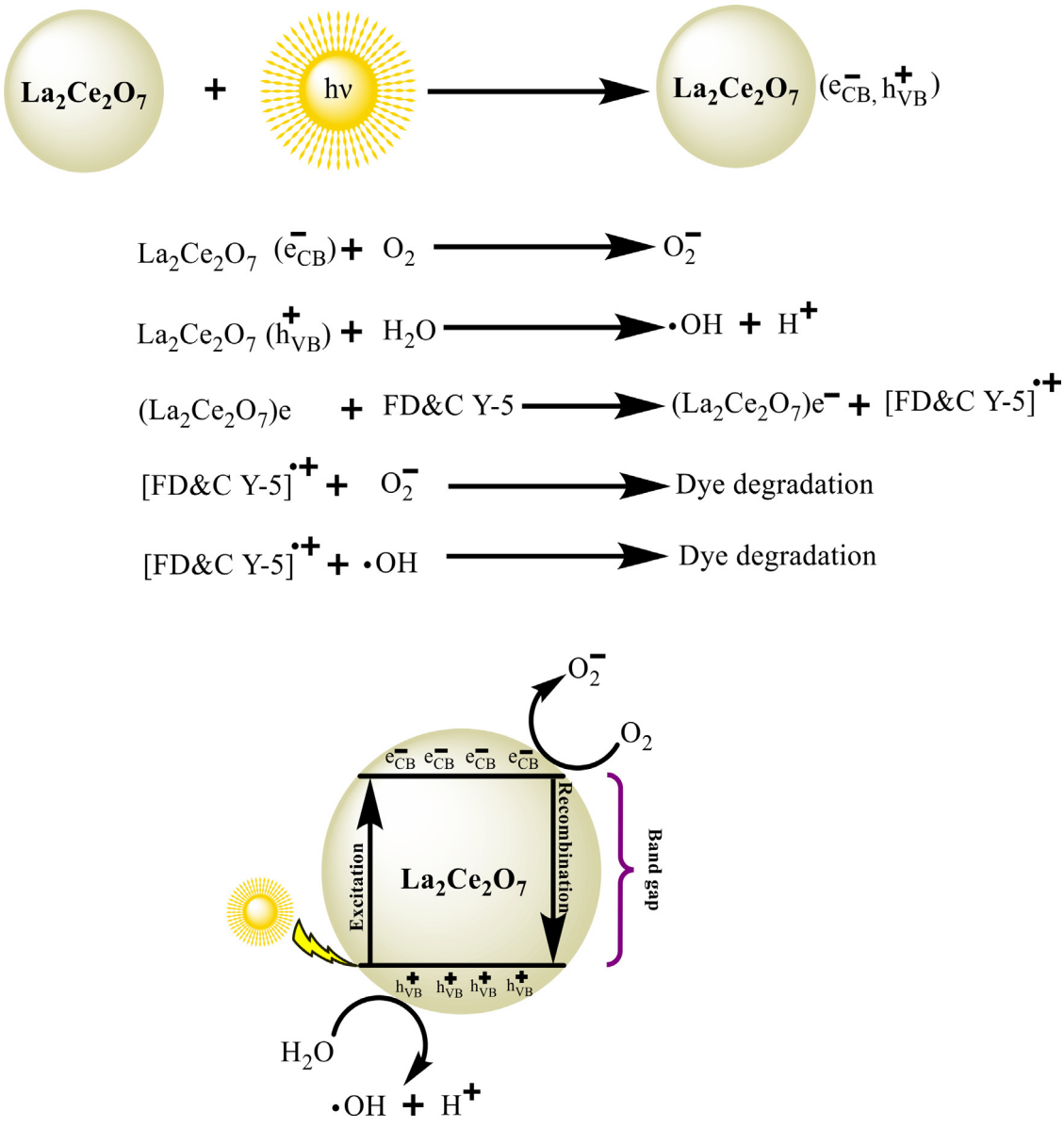

Fig. 10. Plausible mechanistic representation of the $La_2Ce_2O_7$ mediated photocatalytic degradation of FD&C Yellow 5 (For interpretation of the references to color in this figure legend, the reader is referred to the web version of this article.).

investigated as 2.1 eV (the obtained result was consistent with the value reported by Tinwala et al. (2013)), which is low and conducive to the absorption of visible light of higher wavelengths.

5. Conclusions

The present study demonstrates the prospective utilization of lanthanum cerate ($La_2Ce_2O_7$), a perovskite nanomaterial, to remove carcinogenic and neurotoxic dye FDC Yellow 5 from its aqueous solution. Several points have been found out from the several instrument-based assessments such XRD reveals cubic fluorite type structure with space group Fm3m2 suggesting its perovskite structure. BET surface area analysis confirms about meso-porosity, while from SEM and TEM analysis the synthesized perovskite particles found to be plate like flaky structure, with irregular shape, and lots of agglomeration was also evident. Process variables exert a significant influence on the dye removal process. The highest dye uptake of 92% was achieved at pH 2.0, suggesting protonated condition favors the removal of dye species. The mechanism of the removal process was investigated through various kinetics models. The pore diffusion process was found to be more dominating and governed the rate-limiting step. The quantification of the adsorption process was interpreted using different equilibrium models. Freundlich model describes the adsorption data more appropriately. The maximum adsorption capacity of the perovskite material was estimated as 133.3 mg/g at 323 K. The photocatalytic potential of the synthesized perovskite was investigated by evaluating the bandgap as 2.1 eV, which is low and triggers the production of reactive superoxide and hydroxide species which facilitates dye degradation process. Overall, the synthesized perovskite material possesses commendable efficiency and serves as a promising candidate for the sequestration of hazardous colored nuisances from water and wastewater.

Declaration of Competing Interest

None.

Acknowledgment

Dr. Sushmita Banerjee is thankful for the financial assistance in the form of SEED FUND PROJECT (1902-10) by Sharda University, Greater Noida, India. Dr. Bharat Kumar Allam is grateful to Rajiv Gandhi University, Arunachal Pradesh, for providing essential facilities. Authors are also thankful to the anonymous reviewers for their insightful comments and suggestions.

References

Ahmad, M.A., Ahmad Puad, N.A., Bello, O.S., 2014. Kinetic, equilibrium and thermodynamic studies of synthetic dye removal using pomegranate peel activated carbon prepared by microwave-induced KOH activation. Water Resour. Ind. doi:10.1016/j.wri.2014.06.002.

Arrhenius, S., 1889. On the reaction rate of the inversion of non-refined sugar upon souring. Z. Phys. Chem. doi:10.1515/zpch-1889-0416.

Banerjee, S., Chattopadhyaya, M.C., 2017. Adsorption characteristics for the removal of a toxic dye, tartrazine from aqueous solutions by a low cost agricultural by-product. Arab. J. Chem. doi:10.1016/j.arabjc.2013.06.005.

Bilel, C., Jbeli, R., Ben Jemaa, I., Boukhachem, A., Saadallah, F., Amlouk, M., Ezzaouïa, H., 2020. Physical investigations on annealed structure Cu/La_2O_3 for photocatalytic application under sunlight. J. Mater. Sci. Mater. Electron. doi:10.1007/s10854-020-02863-4.

Busca, G., 2009. The use of infrared spectroscopic methods in the field of heterogeneous catalysis by metal oxides. Metal Oxide Catalysis. WILEY-VCH Verlag GmbH & Co. KGaA, Weinheim, Germany doi:10.1002/9783527626113.ch3.

Chiu, Y.H., Chang, T.F.M., Chen, C.Y., Sone, M., Hsu, Y.J., 2019. Mechanistic insights into photodegradation of organic dyes using heterostructure photocatalysts. Catalysts doi:10.3390/catal9050430.

Chukwuemeka-Okorie, H.O., Ekuma, F.K., Akpomie, K.G., Nnaji, J.C., Okereafor, A.G., 2021. Adsorption of tartrazine and sunset yellow anionic dyes onto activated carbon derived from cassava sievate biomass. Appl. Water Sci. doi:10.1007/s13201-021-01357-w.

Deepika, S., Harishkumar, R., Dinesh, M., Abarna, R., Anbalagan, M., Roopan, S.M., Selvaraj, C.I., 2017. Photocatalytic degradation of synthetic food dye, sunset yellow FCF (FD&C yellow no. 6) by Ailanthus excelsa Roxb. possessing antioxidant and cytotoxic activity. J. Photochem. Photobiol. B Biol. doi:10.1016/j.jphotobiol.2017.10.015.

Dimesso, L., 2018. Pechini processes: an alternate approach of the sol-gel method, preparation, properties, and applications. Handbook of Sol-Gel Science and Technology doi:10.1007/978-3-319-32101-1_123.

Ebrahimpoor, S., Kiarostami, V., Khosravi, M., Davallo, M., Ghaedi, A., 2021. Optimization of tartrazine adsorption onto polypyrrole/$SrFe_{12}O_{19}$/graphene oxide nanocomposite using central composite design and bat inspired algorithm with the aid of artificial neural networks. Fiber Polym. doi:10.1007/s12221-021-8163-9.

El-Bindary, A.A., Shoair, A.F., Kiwaan, H.A., Hawas, A.R., 2018. Preparation, characterization, and application of synthesized thiourea formaldehyde-calcium alginate in removal of Reactive Black 5. Can. J. Chem. doi:10.1139/cjc-2017-0767.

Eriksson, P., Tal, A.A., Skallberg, A., Brommesson, C., Hu, Z., Boyd, R.D., Olovsson, W., Fairley, N., Abrikosov, I.A., Zhang, X., Uvdal, K., 2018. Cerium oxide nanoparticles with antioxidant capabilities and gadolinium integration for MRI contrast enhancement. Sci. Rep. doi:10.1038/s41598-018-25390-z.

Gautam, P.K., Shivapriya, P.M., Banerjee, S., Sahoo, A.K., Samanta, S.K., 2019. Biogenic fabrication of iron nanoadsorbents from mixed waste biomass for aqueous phase removal of alizarin red S and tartrazine: kinetics, isotherm, and thermodynamic investigation. Environ. Prog. Sustain. Energy doi:10.1002/ep.13326.

Goscianska, J., Pietrzak, R., 2014. Removal of tartrazine from aqueous solution by carbon nanotubesdecorated with silver nanoparticles. Catal. Today doi:10.1016/j.cattod.2014.11.017.

Hutson, N.D., Yang, R.T., 1997. Theoretical basis for the Dubinin-Radushkevitch (D-R) adsorption isotherm equation. Adsorption doi:10.1007/BF01650130.

Jacob, R., Nair, H.G., Isac, J., 2014. Structural and morphological studies of nanocrystalline ceramic $BaSr_{0\cdot9}Fe_{0\cdot1}TiO_4$. Int. Lett. Chem. Phys. Astron. doi:10.18052/www.scipress.com/ilcpa.41.100.

Jeppu, G.P., Clement, T.P., 2012. A modified Langmuir-Freundlich isotherm model for simulating pH-dependent adsorption effects. J. Contam. Hydrol. doi:10.1016/j.jconhyd.2011.12.001.

Jiang, S.R., Yan, P.X., Feng, B.X., Cai, X.M., Wang, J., 2003. The response of a NiOx thin film to a step potential and its electrochromic mechanism. Mater. Chem. Phys. doi:10.1016/S0254-0584(02)00010-X.

Jung, H.S., Park, N.G., 2015. Perovskite solar cells: from materials to devices. Small doi:10.1002/smll.201402767.

Kishor Kumar, M.J., Kalathi, J.T., 2018. Low-temperature sonochemical synthesis of high dielectric Lanthanum doped Cerium oxide nanopowder. J. Alloy. Compd. doi:10.1016/j.jallcom.2018.03.096.

Klett, C., Barry, A., Balti, I., Lelli, P., Schoenstein, F., Jouini, N., 2014. Nickel doped Zinc oxide as a potential sorbent for decolorization of specific dyes, methylorange and tartrazine by adsorption process. J. Environ. Chem. Eng. doi:10.1016/j.jece.2014.03.001.

Langmuir, D.A.O., 2012. Freundlich, Temkin and Dubinin–Radushkevich isotherms studies of equilibrium sorption of Zn 2+ unto phosphoric acid modified rice husk. IOSR J. Appl. Chem. doi:10.9790/5736-0313845.

McKay, G., Poots, V.J.P., 1980. Kinetics and diffusion processes in colour removal from effluent using wood as an adsorbent. J. Chem. Technol. Biotechnol. doi:10.1002/jctb.503300134.

Mehdizadeh, P., Amiri, O., Rashki, S., Salavati-Niasari, M., Salimian, M., Foong, L.K., 2020. Effective removal of organic pollution by using sonochemical prepared $LaFeO_3$ perovskite under visible light. Ultrason. Sonochem. doi:10.1016/j.ultsonch.2019.104848.

Moussout, H., Ahlafi, H., Aazza, M., Maghat, H., 2018. Critical of linear and nonlinear equations of pseudo-first order and pseudo-second order kinetic models. Karbala Int. J. Mod. Sci. doi:10.1016/j.kijoms.2018.04.001.

Ouassif, H., Moujahid, E.M., Lahkale, R., Sadik, R., Bouragba, F.Z., Sabbar, E.m., Diouri, M., 2020. Zinc-Aluminum layered double hydroxide: high efficient removal by adsorption of tartrazine dye from aqueous solution. Surf. Interfac doi:10.1016/j.surfin.2019.100401.

Banerjee, P.S., Debnath, A., Singh, V., 2021. Gum ghatti-alginate hybrid bead derived titania spheres for deep removal of toxic dye Remazol brilliant violet from aqueous solutions. Environ. Nanotechnol. Monit. Manag. doi:10.1016/j.enmm.2021.100459.

Reck, I.M., Paixão, R.M., Bergamasco, R., Vieira, M.F., Vieira, A.M.S., 2018. Removal of tartrazine from aqueous solutions using adsorbents based on activated carbon and Moringa oleifera seeds. J. Clean. Prod. doi:10.1016/j.jclepro.2017.09.237.

Saeed, T., Naeem, A., Mahmood, T., Ahmad, Z., Farooq, M., Farida, I.U.Din, Khan, I.W., 2021. Comparative study for removal of cationic dye from aqueous solutions by manganese oxide and manganese oxide composite. Int. J. Environ. Sci. Technol. doi:10.1007/s13762-020-02844-4.

Sahnoun, S., Boutahala, M., Tiar, C., Kahoul, A., 2018. Adsorption of tartrazine from an aqueous solution by octadecyltrimethylammonium bromide-modified bentonite: kinetics and isotherm modeling. C. R. Chim. doi:10.1016/j.crci.2018.01.008.

Sellaoui, L., Dhaouadi, F., Li, Z., Cadaval, T.R.S., Igansi, A.V., Pinto, L.A.A., Dotto, G.L., Bonilla-Petriciolet, A., Pinto, D., Chen, Z., 2021. Implementation of a multilayer statistical physics model to interpret the adsorption of food dyes on a chitosan film. J. Environ. Chem. Eng. doi:10.1016/j.jece.2021.105516.

Soltani, T., Entezari, M.H., 2013. Photolysis and photocatalysis of methylene blue by ferrite bismuth nanoparticles under sunlight irradiation. J. Mol. Catal. A Chem. doi:10.1016/j.molcata.2013.05.004.

Srivastava, V., Madyannik, P., Sharma, Y.C., Sillanpaa, M., 2015. Synthesis and application of polypyrrole coated tenorite nanoparticles 1 (PPy@TN) for the removal of anionic food dye 'Tartrazine' and divalent metallic ions viz. Pb(II),Cd(II), Zn(II), Co(II), Mn(II) from synthetic wastewater. RSC Adv. doi:10.1039/c5ra14108g.

Stoyanovskii, V.O., Vedyagin, A.A., Volodin, A.M., Bespalko, Y.N., 2020. Effect of carbon shell on stabilization of single-phase lanthanum and praseodymium hexaaluminates prepared by a modified Pechini method. Ceram. Int. doi:10.1016/j.ceramint.2020.08.088.

Tinwala, H., Shah, D.C., Menghani, J., 2013. Effect of temperature on crystallite size of lanthanum cerium oxide ($La_2Ce_2O_7$) and its optical properties. Carbon Sci. Tech. 5 (1), 225–230.

Védrine, J.C., 2019. Metal oxides in heterogeneous oxidation catalysis: state of the art and challenges for a more sustainable world. ChemSusChem doi:10.1002/cssc.201802248.

Weber, W.J., Morris, J.C., 1963. Kinetics of adsorption on carbon from solution. J. Sanit. Eng. Div. doi:10.1061/jsedai.0000430.

Wei, X., Wang, Y., Feng, Y., Xie, X., Li, X., Yang, S., 2019. Different adsorption-degradation behavior of methylene blue and Congo red in nanoceria/H_2O_2 system under alkaline conditions. Sci. Rep. doi:10.1038/s41598-018-36794-2.

Zhang, F.X., Tracy, C.L., Lang, M., Ewing, R.C., 2016. Stability of fluorite-type $La_2Ce_2O_7$ under extreme conditions. J. Alloy. Compd. doi:10.1016/j.jallcom.2016.03.002.